PCCP

ROYAL SOCIETY OF CHEMISTRY

PAPER

View Article Online
View Journal

Cite this: DOI: 10.1039/d6cp00843g

Excited-state dissociation of (η^4-diene)Ru(CO)$_3$ precursors for photo-assisted chemical vapour deposition

Cauê P. Souza, [a] Alexey V. Verkhovtsev, [b] Amy V. Walker, [c] Nigel J. Mason, [d] Andrey V. Solov'yov, [b] Lisa McElwee-White, [e] Matija Zlatar *[f] and Felipe Fantuzzi *[a]

Ruthenium π-diene carbonyl complexes have emerged as promising precursors for photo-assisted chemical vapour deposition (PACVD), yet their photodissociation mechanisms remain unclear. Here we use static quantum-chemical calculations to map the excited-state dissociation landscape of (η^4-diene)Ru(CO)$_3$ precursors (diene = BuD, MBuD, CHD, COT, CBuD). Ground-state DFT optimisations and Ru–ligand scans are combined with TD-DFT excitations and adiabatic singlet potential energy surface profiles to identify CO- and diene-loss pathways, while EDA–NOCV and natural transition orbital analyses rationalise the Ru–diene bonding and the character of the bright states that drive reactivity. Calculated UV-vis spectra reproduce experimental trends, including the markedly higher absorptivity and extended wavelength coverage of the COT-containing complex. CO loss is generally enabled by a range of ligand-field or charge-transfer excitations and internal conversion-assisted channels. In contrast, diene loss is strongly ligand dependent: BuD, MBuD, and CHD show accessible pathways, CBuD remains resistant, and COT exhibits additional complexity due to ligand flexibility and coordination changes, all consistent with experiment. These results outline favourable stepwise routes towards unsaturated fragments and provide a basis for future non-adiabatic dynamics, irradiation-driven molecular dynamics, time-resolved spectroscopy, and multiscale simulations of PACVD processes.

Received 7th March 2026,
Accepted 18th May 2026

DOI: 10.1039/d6cp00843g

rsc.li/pccp

1 Introduction

Metal–carbonyl complexes are among the earliest and most widely studied precursors for nanofabrication *via* chemical vapour deposition (CVD)[1,2] and, more recently, focused electron beam-induced deposition (FEBID).[3–5] Their successful use in these established techniques has also been extended to photo-assisted CVD (PACVD), a near-room-temperature deposition method in which precursors are activated by photons rather than thermal energy.[1] Conventional CVD of metals and metal-containing compounds is widely employed in microelectronics, semiconductors, optoelectronics, and protective coatings,[6–9] where substrates can tolerate the high pyrolytic temperatures typically required to activate precursors. However, many emerging technologies, including organic photovoltaics,[10] chemical sensors,[11] and related electronic devices,[12,13] rely on thermally sensitive polymeric thin films or self-assembled monolayers (SAMs). As such substrates cannot withstand conventional CVD conditions, PACVD offers an attractive alternative, enabling lower-temperature processing with improved selectivity and energy efficiency. Therefore, understanding the excited-state pathways responsible for precursor activation becomes essential.

Among the various metals of interest for nanofabrication, ruthenium has received much attention in recent decades. It has high thermal resistance (melting point 2273 °C), a high work function (4.7 eV), low bulk resistivity (7.16 μΩ cm), and its only stable solid oxide, RuO_2, is also a metallic conductor (with a resistivity of 35.2 μΩ cm).[2,14] This makes Ru a promising metal for thin film technologies,[15] next-generation capacitors[16] and dynamic random access memory (DRAM) devices.[17] It is also an attractive choice for replacing or enhancing current Cu interconnects in nanoelectronic devices.[18,19] Previous techniques for the preparation of ruthenium films, such as pulsed

[a] School of Natural Sciences, University of Kent, Park Wood Rd, Canterbury CT2 7NH, UK. E-mail: f.fantuzzi@kent.ac.uk
[b] MBN Research Center, Altenhöferallee 3, Frankfurt am Main 60438, Germany
[c] Department of Materials Science and Engineering, University of Texas at Dallas, 800 W. Campbell Rd, Richardson, Texas 75080, USA
[d] School of Engineering, Mathematics and Physics, University of Kent, Park Wood Rd, Canterbury CT2 7NH, UK
[e] Department of Chemistry, University of Florida, Gainesville, Florida 32611, USA
[f] Institute of Chemistry, Technology and Metallurgy, University of Belgrade, Njegoševa 12, Belgrade 11000, Serbia. E-mail: matija.zlatar@ihtm.bg.ac.rs

laser deposition, molecular beam epitaxy, lift-off methods, and electrodeposition, have shown various limitations. CVD and its variations are promising alternatives to overcome these issues.[2,20,21]

A suitable precursor for PACVD must meet key requirements: (i) be highly volatile; (ii) be stable at vaporisation temperatures; (iii) possess high photodissociation quantum yields; and (iv) have facile thermal reactions on the substrate surface for completion of ligand loss. Although many homoleptic metal–carbonyl compounds meet all these criteria while also being simple and commercially available, $Ru(CO)_5$ decomposes above −18 °C.[2] The introduction of hydrocarbon polyhapto ligands in place of one or more CO ligands is one strategy to stabilise the complex while maintaining the remaining desirable properties. Ru–carbonyl compounds containing both η^3 and η^4 ligands have recently shown promising performance in PACVD.[20,22–24] However, the detailed excited-state landscape, the competition between CO and diene loss, and the ligand-dependent accessibility of these channels remain unresolved.

Although the photochemistry of first-row transition metal–carbonyl complexes has been extensively studied, investigations become markedly scarcer for heavier congeners. To the best of our knowledge, the only study to date on the photochemistry of (η^4-diene)$Ru(CO)_3$ complexes [diene = butadiene (BuD), isoprene or 2-methyl-1,3-butadiene (MBuD), cyclooctatetraene (COT), 1,3-cyclohexadiene (CHD), cyclobutadiene (CBuD); Fig. 1] was reported by some of us.[24,25] In that work, **3COT** was excluded from the photolysis experiments because it showed evidence of dissociation products in the dark. The solution-phase investigation revealed loss of both CO and diene upon UV irradiation with a Hg(Xe) arc lamp, identifying these complexes as promising precursors for PACVD of ruthenium. Primary CO loss was observed for all compounds, whereas primary diene loss occurred only for **3BuD** and **3MBuD**. The quantum yields for CO loss were wavelength dependent for all compounds except **3BuD**, and diene loss showed a similar wavelength dependence for **3BuD** and **3MBuD**. Extended photolysis produced species consistent with loss of one CO, loss of diene, loss of two CO, and combined CO/diene loss for all complexes except **3BuD**, for which only one- and two-CO loss products were detected. With the exception of **3BuD**, exhaustive photolysis yielded colloidal Ru. DFT calculations indicated that these photodissociation processes originate from ligand-field (LF) excited states, and **3BuD** and **3MBuD** emerged as the most promising candidate precursors.

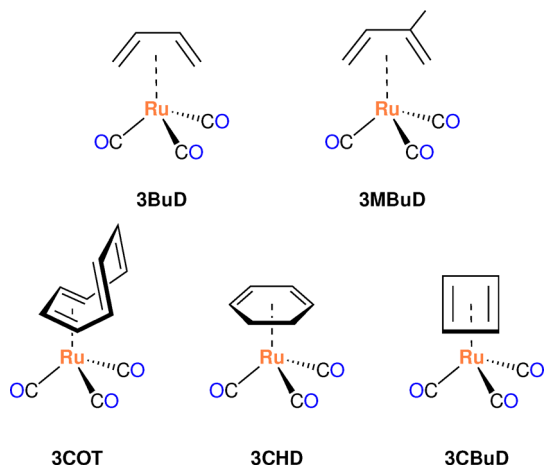

Fig. 1 (η^4-Diene)$Ru(CO)_3$ compounds investigated in this study and previously in ref. 24.

It is clear that photochemical studies of Ru–carbonyl complexes remain scarce, and even the prototypical $Ru(CO)_5$ has not been extensively investigated. In contrast, related iron systems are much better characterised, and we briefly summarise the most relevant findings for (η^4-diene)$Fe(CO)_3$ complexes and $M(CO)_5$ (M = Fe, Ru). Jaenicke *et al.*[26] examined the solution-phase photolysis of several (η^4-diene)$Fe(CO)_3$ and (η^4-diene)$_2$Fe(CO) complexes, finding wavelength-dependent CO loss that exceeds diene loss by roughly an order of magnitude and increases at shorter wavelengths; transient (η^2-diene) species were also detected. Bachler *et al.*[27] observed similar $\eta^4 \rightarrow \eta^2$ photoisomerisation and *cis–trans* isomerisation in (BuD)$Fe(CO)_3$, while Chang and Zink[28] reported wavelength-dependent CO and diene loss from (COT)$Fe(CO)_5$ with smaller differences between the respective quantum yields. The homoleptic carbonyls $M(CO)_5$ provide additional context: $Fe(CO)_5$ undergoes rapid loss of up to two CO ligands after single-photon absorption, with further dissociation depending on photon energy.[29–31] Complete CO loss can occur in the gas phase or inert matrices,[29] and the process is strongly wavelength dependent.[32] Dissociation generally proceeds stepwise, though concerted multi-CO loss *via* multiphoton absorption has been reported.[29,32] Vibrational quenching in solution reduces overall dissociation,[29,31,33] and both experiment and theory indicate that the first CO losses occur primarily on the singlet manifold,[31,34] with possible triplet involvement in later steps.[35] Reactive fragments such as $Fe(CO)_2$ and Fe(CO) can further react with the parent complex to form polynuclear species.[29]

In contrast, photolysis of $Ru(CO)_5$ produces $Ru(CO)_4$, which readily recombines with CO to regenerate the parent complex.[36] The compound is thermally unstable[2] and can also form $Ru_3(CO)_{12}$ photochemically.[36,37] A further distinction is that unsaturated $Fe(CO)_n$ fragments (n = 4–1) have triplet ground states (GS),[29,31,34] whereas the Ru analogues (Ru(CO) excepted) are singlets.[36–38] The heavier Ru centre is also expected to exhibit stronger spin–orbit coupling, although quantitative data remain limited.

In this work, we build upon the previous investigation[24] of the photochemistry of (η^4-diene)$Ru(CO)_3$ complexes (Fig. 1) using static quantum-chemical methods to further elucidate the photodissociation pathways of these precursors, in line with established strategies for modelling excited states in organometallic systems.[39,40] A comparison of geometrical parameters, bonding descriptions, excited states, and energetic profiles of the pristine complexes and their fragments, together with selected ground- and excited-state potential energy surface sections, helps clarify the mechanisms of ligand loss and

provides guidance for the design of improved PACVD ruthenium precursors. Where appropriate, we also compare the Ru complexes to their iron analogues. An additional objective is to establish a foundation for multiscale modelling of PACVD through molecular dynamics simulations. A workflow previously developed for evaluating and selecting CHARMM force-field parameters for realistic simulations of alkanethiol SAM substrates[41] will be extended here, and the present results will support parametrisation of reactive CHARMM (rCHARMM)[42] force fields for the precursors. Such parametrisation is required for future irradiation-driven molecular dynamics (IDMD)[43,44] simulations with the MBN Explorer[45] package within a broader multiscale framework for radiation–matter interactions,[46] an approach already successfully applied to FEBID processes involving related precursors such as $W(CO)_6$,[43,47,48] $Fe(CO)_5$,[33,49] and other organometallic compounds.[50–52]

2 Computational methods

For all compounds investigated here, geometry optimisation and TD-DFT vertical transition calculations were performed using the range-separated functional ωB97X[53] with Grimme's D3 dispersion correction.[54] The Weigend & Ahlrichs def2-TZVP basis set with effective core potential (ECP) was used on the Ru atoms, while the smaller def2-SVP basis set was used for all other atoms.[55] This level of theory was applied to all scans. To perform a rigid scan of the Ru–diene bonds, we stretched and contracted the equilibrium distance between the diene and the $Ru(CO)_n$ moieties along the line joining the metal to the centroid of the four carbon atoms involved in the η^4 (or the six in the case of η^6) coordination. A contraction of 0.5 Å was used in all cases, while stretching was extended as far as needed to reach the dissociation plateau. Steps of 0.1 Å were used in all scans. At each point in the scans, vertical excitations *via* TD-DFT for 30 singlet and 30 triplet states were calculated. These calculations were performed using Gaussian 16 Rev A.03.[56]

For the CBuD- and COT-containing complexes, Ru–diene dissociation pathways were also explored using the nudged elastic band (NEB) method.[57] The initial structure corresponded to the equilibrium geometry with the Ru–diene distance shortened by 0.5 Å along the vector connecting Ru to the centroid of the four coordinating carbon atoms. The final structure was generated by elongating the same coordinate by 1.8 Å from equilibrium and replacing the bound diene with the optimised isolated ligand while keeping the centroid coincident. At each image point in the converged path, vertical TD-DFT excitations were obtained for 30 singlet and 30 triplet states. All NEB calculations were carried out with ORCA 5.0.3[58] using ωB97X together with the D3 dispersion correction and Becke–Johnson damping (D3BJ).[59] The split basis-set scheme described above and the RIJCOSX approximation with def2 auxiliary basis sets were employed.[60] Transition states associated with possible changes in COT coordination (see Section 3.1) were located using the NEB-TS variant[61] at the same level of theory, with reactant and product geometries optimised prior to the NEB-TS calculations.

To aid in the interpretation of the electronic transitions, the natural transition orbital (NTO) analysis[62,63] *via* the TheoDORE package[64] was used on the Gaussian 16-generated orbitals. Simulated absorption spectra were obtained by applying artificial broadening[65] to the TD-DFT transitions (see Section S1, SI).

The energy decomposition analysis with natural orbitals for chemical valence (EDA–NOCV)[66] was performed using the Amsterdam density functional (ADF)[67] module of the Amsterdam modeling suite (AMS)[68] v 2024.101 to characterise the Ru–diene interactions. The diene (BuD, MBuD, COT, CHD, or CBuD) and the remaining fragment were treated as separate moieties, and five fragmentation schemes were tested: (1) neutral singlets, (2) neutral triplets, (3) doublet fragments with charges ±1, (4) singlet fragments with charges ±2, and (5) triplet fragments with charges ±2. All calculations employed the PBE0 functional[69] with D4 dispersion,[70] TZ2P basis set,[71] and scalar relativistic ZORA corrections.[72]

3 Results and discussion

This section is organised as follows. Section 3.1 presents the equilibrium GS geometries of the precursors and their fragments, followed by an analysis of Ru–diene bonding using EDA–NOCV (Section 3.2). Computed UV-vis spectra and assignment of key transitions *via* NTO analysis concludes the preamble in Section 3.3.

We then examine the photodissociation pathways through (TD-)DFT potential energy surface scans for Ru–ligand bond cleavage, presented in the adiabatic picture with excited states referenced to their ordering at the GS equilibrium geometry. Fig. 2 summarises all pathways from the pristine precursors to bare Ru and serves as a guide for the discussion. Section 3.4 addresses diene loss from pristine precursors and fragments (steps 2, 2.1, 2.3, and 2.5 in Fig. 2), followed by CO loss from diene-containing species (steps 1, 2.2, and 2.4) in Section 3.5. Section 3.6 examines CO loss from the $Ru(CO)_n$ fragments (steps 1.1–1.3). The section concludes with the proposed exhaustive dissociation pathways for the three most thoroughly analysed systems, **3COT**, **3BuD**, and **3CBuD** as supported by the current method (Section 3.7). In the ensuing discussion, the proposed pathways should be regarded as a subset of the channels accessible within the coordinates explored here. Additional geometrical degrees of freedom may open alternative routes that require more detailed dynamical investigations beyond the scope of this work.

3.1 Equilibrium geometries of pristine precursors and their fragments

Before analysing the photodissociation pathways, we briefly summarise the GS equilibrium geometries of the precursors and their fragments. For **3COT**, **3BuD**, and **3CBuD**, full dissociation sequences to bare Ru were explored through

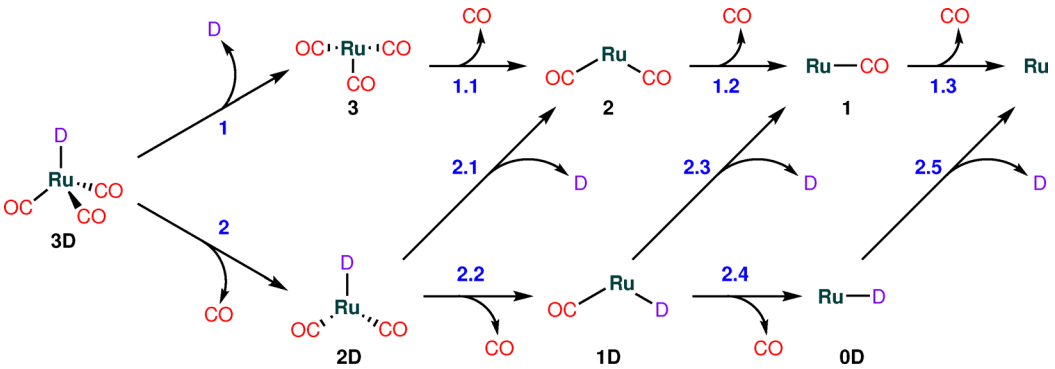

Fig. 2 General exhaustive dissociation pathways for (η^4-diene)Ru(CO)$_3$ compounds. D = diene. Only **3COT**, **3BuD**, and **3CBuD** were considered for the total dissociations. For **3MBuD** and **3CHD**, only the primary dissociations of diene and CO (*i.e.* steps 1 and 2) were considered.

Ru–ligand bond scans, whereas for **3MBuD** and **3CHD**, only the first CO and diene losses were considered. Fig. 3 shows the optimised geometries of all species. With the exception of Ru(CO) (**1**), all have singlet GS well below the lowest triplets if they exist (see also Table S1, SI); the smallest gap is 3.4 kcal mol^{-1} (0.15 eV) for C_{2v} Ru(CO)$_2$ (*vide infra*). All pristine precursors except **3MBuD** adopt C_s symmetry, as do most fragments, with a few notable exceptions discussed below.

Loss of the diene at any stage of the dissociation sequence generates Ru(CO)$_n$ fragments, common to all precursors. Fragment **1** (n = 1) adopts the expected linear triplet GS ($C_{\infty v}$), with the singlet lying 24.7 kcal mol^{-1} (1.07 eV) higher in energy. Fragment **2** (***n*** = 2) has a singlet C_{2v} GS with a small singlet–triplet gap to the lowest-lying triplet state (C_{2v}) of 3.4 kcal mol^{-1} (0.15 eV). In turn, fragment **3** (***n*** = 3) adopts a singlet C_s GS with a 7.8 kcal mol^{-1} (0.34 eV) gap to the lowest triplet (C_{2v}). These trends contrast markedly with the Fe analogues: all unsaturated Fe(CO)$_n$ fragments have triplet GS and Fe(CO)$_2$ is linear ($D_{\infty h}$), as established by experiments and theory.[29,31,34,35] From our calculations, even the triplet state of the Ru analogue **2** has C_{2v} symmetry. These differences are consistent with established trends between first- and second-row transition metals, where the greater spatial extent and polarisability of 4d orbitals, together with relativistic effects, can lead to distinct metal–ligand bonding patterns and structural preferences.[73–75]

Fragment **3** and its analogue Fe(CO)$_3$ are interesting cases. In both cases, the triplet C_{2v} and C_{3v} geometries are nearly degenerate, differing by 0.9 kcal mol^{-1} (0.04 eV) for Fe(CO)$_3$ and only 0.3 kcal mol^{-1} (0.01 eV) for **3**. Our calculations favour the C_{2v} geometry in both cases, although a triplet C_{3v} GS has previously been assigned for Fe(CO)$_3$.[29,31] Given the very small energy separation, such assignments are uncertain. Indeed, Troß *et al.*[35] argued that the two structures for Fe(CO)$_3$ interconvert readily and likely coexist in equilibrium, with DFT and CCSD(T) results differing on the preferred geometry. This ambiguity is unlikely to affect the Ru-containing precursors considered here. Table 1 summarises the singlet and triplet geometries and relative energies of the Ru(CO)$_n$ fragments and their Fe analogues.

For the diene-containing fragments, two points are worth noting. First, the CBuD ligand is a perfect square in **0CBuD** and **1CBuD**, but becomes slightly deltoid (kite shaped) in **2CBuD** and **3CBuD** owing to the out-of-symmetry-plane carbonyl groups. In **3CBuD**, adjacent C–C bonds measure 1.44 Å and 1.46 Å, while in **2CBuD** they are 1.43 Å and 1.48 Å. Second, η^4-coordinated dienes may in principle convert to η^2 coordination under UV irradiation, as observed experimentally for (η^4-diene)Fe(CO)$_3$. However, rapid reversion to η^4 prevents trapping of such intermediates in solution.[26] For this reason, these structures were not considered here.

The remaining structural nuance concerns the COT-containing species, whose ligand offers greater flexibility in metal coordination. Because of the four double bonds, three coordination modes are possible for the singlet GS of

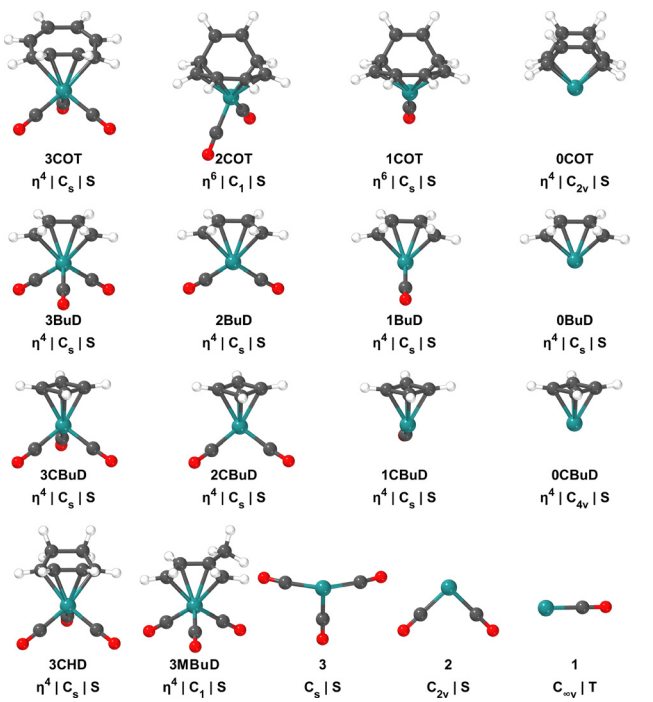

Fig. 3 Optimised GS geometries of the precursors and fragments at the DFT/ωB97X-D3/def2-SVP,def2-TZVP(Ru)+ECP level of theory. Labels indicate diene coordination (except for the Ru(CO)$_n$ fragments), point-group symmetry, and electronic multiplicity (S = singlet, T = triplet).

Table 1 Calculated relative SCF energies, in kcal mol^{-1} (eV) and $\langle S^2 \rangle$ (for triplets), for the various geometries and electronic multiplicities of M(CO)$_n$ fragments (M = Ru, Fe; n = 3, 2, 1) at the DFT/ωB97X-D3/def2-SVP,def2-TZVP(M)+ECP level of theory

			Ru(CO)$_n$		Fe(CO)$_n$	
n	Symm.	Mult.	Energy	$\langle S^2 \rangle$	Energy	$\langle S^2 \rangle$
3	C_s	Singlet	0.00 (0.00)		20.66 (0.90)	
	D_{3h}	Singlet	49.92 (2.16)		31.05 (1.35)	
	C_{2v}	Triplet	7.79 (0.34)	2.010	0.00 (0.00)	2.062
	C_{3v}	Triplet	8.13 (0.35)	2.008	0.90 (0.04)	2.107
2	C_{2v}	Singlet	0.00 (0.00)		34.87 (1.51)	
	$D_{\infty h}$	Singlet	31.46 (1.36)		32.01 (1.39)	
	C_{2v}	Triplet	3.41 (0.15)	2.013	20.03 (0.87)	2.378
	$D_{\infty h}$	Triplet	6.70 (0.29)	2.020	0.00 (0.00)	2.097
1	$C_{\infty v}$	Singlet	24.66 (1.07)		35.56 (1.54)	
	$C_{\infty v}$	Triplet	0.00 (0.00)	2.033	0.00 (0.00)	2.531

(COT)Ru(CO)$_n$ precursors: edge η^4 (1, 2, 3, 4), centre η^4 (1, 2, 5, 6), and η^6 coordination, although not all fragments support all arrangements. We therefore identify which of these geometries are relevant for the subsequent analysis of the dissociation pathways. Fig. 4 shows the lowest-energy singlet structures and their respective nearest minima, with Fe analogues included for comparison. The pristine **3COT** precursor admits two C_s η^4 isomers (edge and centre), with the edge form lower in energy by 10.8 kcal mol^{-1} (0.47 eV), consistent with crystallographic data for (COT)Fe(CO)$_3$[28,76] and with our calculated separation of 12.7 kcal mol^{-1} (0.55 eV) for the iron analogue. Although COT–Ru complexes can be fluxional,[77] only the lowest-energy structures were retained for the dissociation analysis. No triplet η^4 minima were located for either metal, though η^2-coordinated structures (not shown) exist.

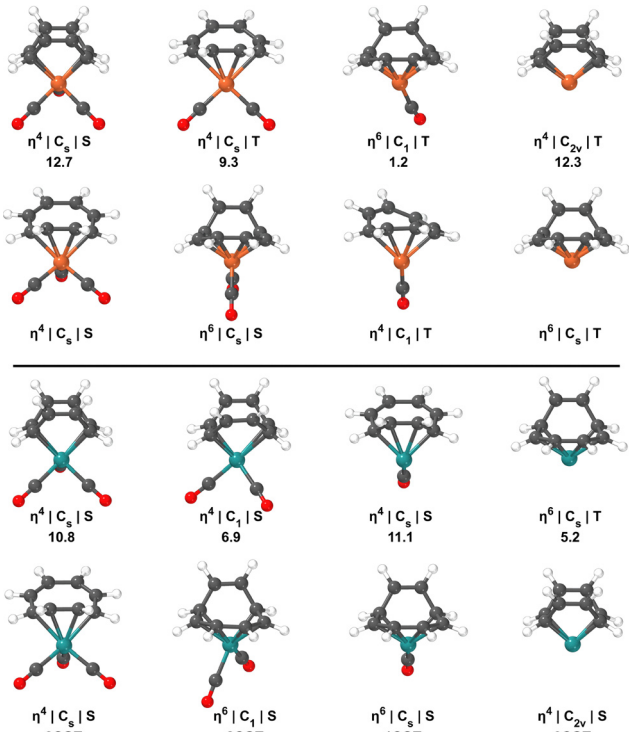

Fig. 4 Optimised global minimum and lowest-lying geometries of the COT-containing precursors and fragments at the DFT/ωB97X-D3/def2-SVP,def2-TZVP(M)+ECP level of theory (M = Ru, Fe). Top: Fe complexes. Bottom: Ru complexes. Labels indicate diene coordination, point-group symmetry, and electronic multiplicity (S = singlet, T = triplet). Relative energies (in kcal mol^{-1}) are given with respect to the corresponding global minimum structure for each species, which is set to zero (first row in each series).

After loss of one CO from **3COT** to form **2COT**, the initially unstable η^4-coordinated fragment relaxes to an η^6 C_s structure; NEB calculations indicate this conversion is barrierless (Fig. S1, SI). The alternative centre-coordinated minimum lies 6.9 kcal mol^{-1} (0.30 eV) higher in energy and is distorted (C_1 symmetry). The Fe analogue (COT)Fe(CO)$_2$ also has a singlet η^6 C_s GS, but in contrast to the Ru system, the next-lowest energy structure is a triplet η^4 edge-coordinated species, reflecting the greater energetic competitiveness of triplet states in the Fe series.

Further CO loss from **2COT** yields **1COT**, which retains an η^6 C_s GS; a centre-coordinated η^4 minimum lies 11.1 kcal mol^{-1} (0.48 eV) above. The Fe analogue instead adopts a distorted triplet η^4 edge-coordinated GS (C_1 symmetry), with a triplet η^6 structure only 1.2 kcal mol^{-1} (0.05 eV) above. Final CO loss gives **0COT**, which undergoes a further rearrangement: the unstable η^6 structure converts to a centre-coordinated η^4 C_{2v} minimum *via* a small barrier of 2.9 kcal mol^{-1} (0.13 eV) (Fig. S2, SI). The closest higher-energy structure is the triplet η^6 (5.2 kcal mol^{-1}, 0.23 eV above). The Fe analogue remains a triplet η^6 C_s species, with a triplet centre-coordinated η^4 structure 12.3 kcal mol^{-1} (0.53 eV) higher. Complete structural and energetic data for all Ru and Fe complexes are provided in Fig. S3 in the SI.

3.2 The diene–Ru bonding

While M–CO bonding has been extensively investigated in transition-metal chemistry,[78,79] the nature of the Ru–diene interaction is less well established. To characterise this interaction, we performed EDA–NOCV fragment analyses in which each complex was partitioned into the diene ligand and the remaining Ru(CO)$_3$ unit. Several coupling schemes were explored (see Section 2), but in all cases the bonding is best described in terms of neutral fragments combined either as singlets or as triplets. Within the EDA–NOCV framework, the most appropriate description corresponds to the scheme yielding the smallest absolute total orbital interaction energy.[80,81] This indicates that the selected fragmentation scheme provides a description of the fragments that is closest to the electronic structure in the bonded system, as it requires the smallest orbital reorganisation upon bond formation, and therefore offers the most appropriate representation of the bonding pattern. This criterion assigns **3COT** and **3CBuD** to a triplet-fragment description, whereas the remaining complexes are better described by singlet fragments (see Section S3, SI for numerical values). This difference can be rationalised in terms of the ligand's HOMO–LUMO gaps (see Table S4, SI). COT and CBuD are the ligands with the smallest HOMO–LUMO gaps when isolated, both in their relaxed and in their bonded geometries, making their triplets closer in energy to their singlets in comparison with the others. A more detailed

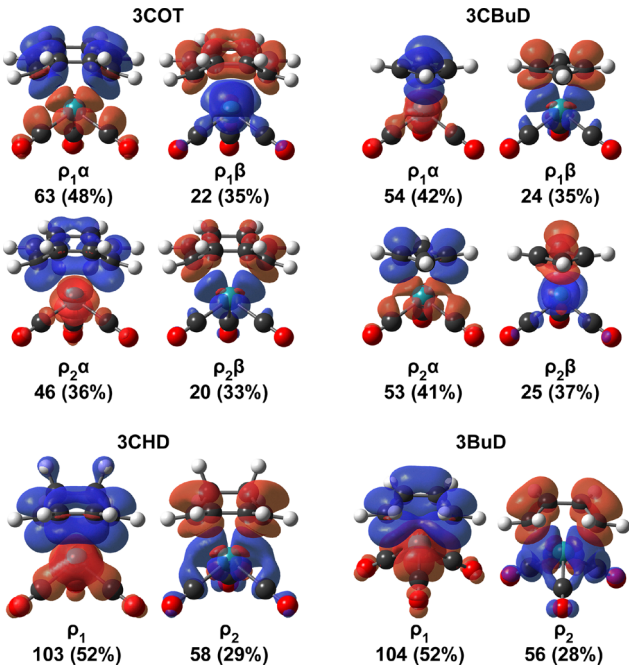

Fig. 5 EDA–NOCV deformation densities (ρ) describing the interaction between diene and $Ru(CO)_3$ fragments. Contributions to the total orbital interaction energy (kcal mol^{-1} and percentage) are given below each density. For triplet-fragment cases (**3COT** and **3CBuD**), percentages refer to each spin component. **3MBuD** is similar to **3BuD** and is omitted. Charge flows from red to blue. Isovalues: 0.002 a.u. Level of theory: SR-ZORA-DFT/PBE0-D4/TZ2P.

discussion of the energy decomposition will be presented elsewhere; here, we focus on qualitative features relevant to the photochemistry.

The deformation densities in Fig. 5 show that, in all complexes, the Ru–diene interaction is dominated by the frontier orbitals of the two fragments. On the ligand side these correspond to π orbitals formed from the sp^2 carbon p orbitals, while on the metal fragment they are Ru d orbitals with some contribution from the CO ligands. In the systems best described by triplet fragments (**3COT** and **3CBuD**), the interaction follows an electron-sharing pattern, with complementary transfer of electron density between singly occupied orbitals on the diene and metal fragments. For the remaining complexes, described by singlet fragments, the interaction instead follows a donor–acceptor pattern, involving donation from the diene HOMO to a metal-centred orbital and backdonation from a metal-centred orbital into the diene LUMO. In both cases, the dominant contributions arise from frontier and low-lying orbitals, so electronic excitation from these orbitals is expected to weaken or disrupt the Ru–diene interaction.

The preference for a triplet-fragment description in **3CBuD** is consistent with the electronic structure commonly attributed to cyclobutadiene in transition-metal complexes. Singlet cyclobutadiene is antiaromatic in a square geometry and therefore tends to distort, whereas a square or near-square geometry can be stabilised by coordination and is often rationalised in terms of triplet (Baird-type) aromaticity.[82–84] The near-square CBuD ligand in **3CBuD**, together with its small HOMO–LUMO gap, is therefore compatible with a triplet-fragment description of the Ru–CBuD interaction. The corresponding result for **3COT** is less straightforward because COT is conformationally flexible and can avoid simple planar antiaromaticity through structural distortion. Nevertheless, its extended π system and small HOMO–LUMO gap may also bring the ligand triplet closer in energy to the singlet and favour an electron-sharing description in the EDA–NOCV analysis. For present purposes, it suffices to note that, irrespective of whether the interaction is best described in donor–acceptor or electron-sharing terms, the Ru–diene bonding in all cases involves frontier orbitals that are susceptible to electronic excitation, supporting the expectation that photoexcitation will facilitate diene dissociation.

3.3 Absorption spectra of the pristine precursors

It is also useful to consider the absorption spectra of the pristine precursors and the character of their main transitions when discussing dissociation pathways. The top panel of Fig. 6 shows the calculated gas-phase spectra. Experimental spectra in heptane have been reported previously.[24,85] Although no solvent effects were included in the calculations, qualitative comparisons with solution spectra remain possible given the close match between experimental and calculated spectra. We

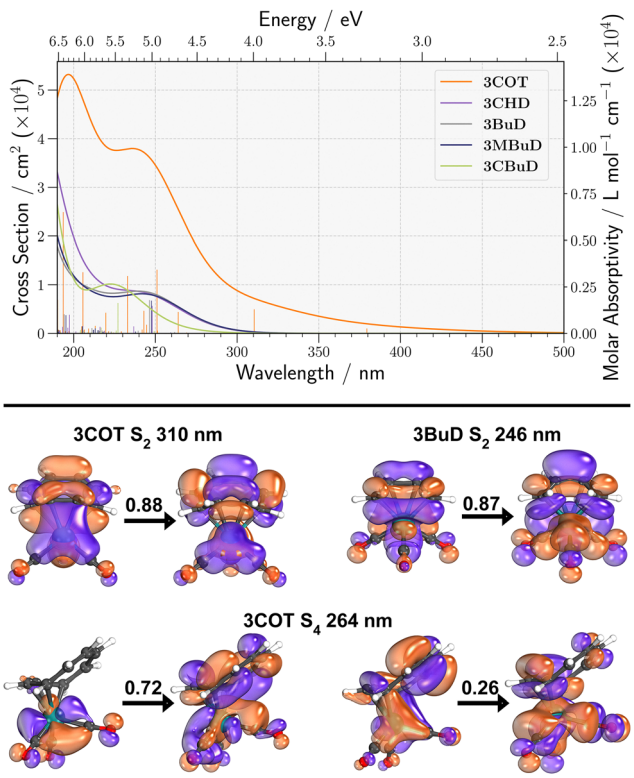

Fig. 6 Top: calculated spectra for the pristine (η^4-diene)$Ru(CO)_3$ considered in this work. The spectral envelopes are Gaussians with σ = 0.4 eV. Bottom: NTOs for selected electronic transitions representing distinct characters (see Table 2). Values over the arrows are the occupation transfer of each orbital pair in the transitions. NTOs are represented as 80% of the density. Level of theory: TD-DFT/ωB97X-D3/def2-SVP,def2-TZVP(Ru)+ECP.

expect solvent effects to minimally shift transition energies and, given the PACVD context, gas phase spectra are more realistic tools. The most striking feature is the distinct spectrum of **3COT**, which displays substantially higher absorptivity across the whole wavelength range and is the only complex with absorption extending into the visible region. This enhanced absorptivity can be attributed to the extended π-conjugation of the COT ligand, which increases electronic delocalisation and leads to a larger number of allowed transitions with higher oscillator strengths, consistent with the experimentally observed higher molar absorptivity of (COT)Ru(CO)$_3$ relative to the other (η^4-diene)Ru(CO)$_3$ precursors.[85] The remaining precursors show similar spectral profiles among themselves, with **3BuD** having the most compact absorption range, consistent with experiment.

The main transitions are summarised in Table 2 and assigned from NTO analysis (full set in Section S4, SI). Transitions with oscillator strength below 0.01 were treated as forbidden. Because the PACVD experiments employed a 500 W Hg(Xe) arc lamp,[24,85] only transitions above 225 nm were considered relevant and are highlighted in bold. With the exception of **3COT**, the active transitions are predominantly ligand-field (LF) in character, involving Ru d orbitals together with CO and diene π/σ orbitals. The relative ligand contributions vary: in **3CHD** and **3CBuD**, CO orbitals dominate at lower energy and diene contributions increase at higher energy, whereas the opposite trend is found for **3BuD** and **3MBuD**. For this latter pair, an additional charge-transfer transition appears near 210–215 nm. In **3BuD**, this transition has ligand-to-ligand charge-transfer (LLCT) character between diene and CO orbitals, whereas in **3MBuD** it combines LLCT with LF contributions. No clear metal-to-ligand charge-transfer (MLCT) transition is found for **3BuD**, in contrast to suggestions for the analogous iron complex.[26]

Precursor **3COT** differs markedly. Its lower-energy transitions are mainly LF but involve strong diene contributions with little CO participation. The S_2 transition (Fig. 6, bottom panel) promotes electron density from an orbital bonding all ligands to one antibonding for the Ru–diene interaction. A further transition at 264 nm (S_4) shows mixed MLCT (to COT) and LLCT character, comparable to the MLCT feature reported for (COT)Fe(CO)$_3$.[28] At higher energy, LLCT contributions become more prominent. **3COT** also exhibits a larger number of allowed transitions above 225 nm (six *versus* one or two for the other precursors). Overall, these assignments are consistent with previous analyses.[24,85]

The relevance of these transitions to photodissociation becomes apparent when compared with the EDA–NOCV description of the bonding. Most LF excitations promote electron density from orbitals contributing to metal–ligand bonding into antibonding combinations, thereby weakening the Ru–ligand interactions. As a result, excitation can lower dissociation barriers and, in some cases, access nonbonded or directly dissociative states, as discussed in the following sections.

3.4 Loss of diene from pristine precursors and fragments

Having established the equilibrium geometries and absorption features of the precursors, we now examine diene-loss pathways (steps 2, 2.1, 2.3 and 2.5 in Fig. 2). The discussion is restricted to singlet excited states, as scans on the triplet surfaces rarely reveal accessible dissociative channels and generally involve barriers too high to compete under the present conditions. For related iron carbonyl systems, the involvement of triplet manifolds in ligand dissociation is also minor.[35] In addition, no phosphorescence was observed in solution-phase photochemical experiments for the present precursors,[24] indicating limited population of long-lived triplet states. These observations suggest that, even if accessed *via* spin–orbit coupling, triplet states are unlikely to provide competitive dissociation pathways due to the associated barriers. Accordingly, the dominant photodissociation pathways are expected to proceed on the singlet manifold under conditions relevant to PACVD. A complete assessment of the role of triplet states, however, would require explicit treatment of spin–orbit coupling and non-adiabatic dynamics, which lies beyond the scope of the present work.

Substitution chemistry has been reported for **3COT** in the dark in the presence of phosphites,[24] motivating consideration of thermal diene loss. In the intact complex, the COT ligand adopts a chair conformation, whereas the free ligand relaxes to a boat structure; dissociation therefore involves substantial conformational reorganisation. Rigid Ru–COT scans reflect this distortion showing GS instabilities at larger separations, consistent with near-degeneracies with low-lying singlet excited states. NEB calculations connecting the equilibrium structure to a geometry with an elongated Ru–COT distance and a relaxed boat COT ligand yield excited-state curves with lower dissociation energies compared to the rigid scans (see Fig. S8, SI),

Table 2 Summary of relevant excitations for the pristine precursors considered in this work. Only transitions with oscillator strength above 0.01 (cross sections $> 1 \times 10^{-18}$ cm^2; molar absorptivities > 286 L mol^{-1} cm^{-1}) are included. Transitions in bold lie above the 225 nm wavelength cut-off of the Hg(Xe) arc lamp. In the Character column, ligands in italics have the major contributions. LF = ligand field; MLCT = metal-to-ligand charge transfer; LLCT = ligand-to-ligand charge transfer

	Wl./nm	f	State	Character
3COT	**310**	**0.0453**	**S_2**	**LF (COT)**
	264	**0.0403**	**S_4**	**MLCT (COT), LLCT (COT to COs)**
	251	**0.1197**	**S_6**	**LF (COT)**
	245	**0.0163**	**S_7**	**LF (COT)**
	243	**0.0424**	**S_8**	**LF (COT)**
	233	**0.1078**	**S_{11}**	**LF (COT)**
	220	0.0388	S_{16}	LLCT (COT to COs), LF (COs)
	206	0.1150	S_{24}	LF (*COT* and *COs*), LLCT (COT to COs)
	194	0.2274	S_{30}	LF (*COT* and *COs*)
3CHD	**248**	**0.0516**	**S_2**	**LF (CHD and *COs*)**
	237	**0.0132**	**S_3**	**LF (CHD and *COs*)**
	216	0.0124	S_{11}	LF (*CHD* and *COs*)
	206	0.0134	S_{15}	LF (*CHD* and *COs*)
3BuD	**246**	**0.0627**	**S_2**	**LF (*BuD* and *COs*)**
	211	0.0100	S_{13}	LLCT (BuD to COs; COs to BuD)
	206	0.0123	S_{15}	LF (BuD and *COs*)
3MBuD	**248**	**0.0616**	**S_2**	**LF (*MBuD* and *COs*)**
	205	0.0133	S_{15}	LF (MBuD and *COs*)
3CBuD	**227**	**0.0571**	**S_5**	**LF (CBuD and *COs*)**
	217	0.0109	S_{10}	LF (*CBuD* and *COs*)

Table 3 Selected bond dissociation energies (BDEs) for all fragmentation pathways investigated in this work. The numbers below each species indicate the dissociation step as defined in Fig. 2. GS = ground state, GS BDE obtained from the optimised geometries of reactants and products; ZPE = zero-point energy; BS = bright state; D_0 = dissociation energy from the bottom of potential energy curve to dissociation plateau; NA = not available, meaning no alternative lower energy pathway including internal conversion exists. All values are SCF energies in kcal mol^{-1}. Except when indicated otherwise, D_0 values were obtained from rigid scans

	GS	GS (+ZPE)	GS D_0	Lowest BS D_0	Lowest effective D_0		GS	GS (+ZPE)	GS D_0	Lowest BS D_0	Lowest effective D_0
3COT						**3CBuD**					
1	63	60	212	10 (S_2)[a]	NA	1	107	104	234	54 (S_5)[a]	NA
2	39	36	44	9 (S_2)	0 (S_6–S_3)	2	49	46	50	23 (S_5)	0 (S_5–S_3)
2.1	65	63	102	36 (S_7)[a]	NA	2.1	99	97	154	49 (S_8)[a]	NA
2.2	37	34	44	26 (S_5)	0 (S_7–S_4)	2.2	50	47	49	9 (S_6)	0 (S_8–S_4)
2.3	76	74	137	80 (S_3)	NA	2.3	97	94	227	73 (S_1)[a]	NA
2.4	54	51	74	44 (S_3)	NA	2.4	54	52	53	36 (S_{10})	0 (S_{10}–S_8)
2.5	88	88	161	95 (S_8)	NA	2.5	109	107	187	82 (S_6)[a]	NA
3BuD						**3CHD**					
1	71	68	138	64 (S_2)	46 (S_2–GS)	1	67	65	141	68 (S_2)	47 (S_2–GS)
2	48	45	47	0 (S_2)	0 (S_2)	2	48	45	47	0 (S_1)	0 (S_2–S_1)
2.1	64	62	94	46 (S_8)	22 (S_4–S_1)						
2.2	43	40	50	23 (S_8)	0 (S_8–S_7)	$Ru(CO)_3$					
2.3	68	66	149	97 (S_4)	71 (S_4–GS)	1.1	41	39	44	20 (S_4)	12 (S_{12}–S_9)
2.4	57	55	60	25 (S_8)	0 (S_8–S_5)	1.2	47	44	70	31 (S_{12})	NA
2.5	77	76	169	100 (S_{16})	NA	1.3	67	65	72	23 (T_9)	0 (T_9–GS)
3MBuD											
1	72	69	141	67 (S_2)	45 (S_2–GS)						
2	47	45	40	0 (S_2)	NA						

[a] Values estimated from NEB MEP (see Section 5, SI).

highlighting the importance of ligand relaxation during dissociation. When it is possible to safely infer on D_0 values from NEB MEP, this has been included in Table 3.

Besides the low BDE for Ru–diene from **3COT**'s S_2 state, the Ru–diene and Ru–CO GS BDEs in **3COT** are among the smallest in the series (Table 3), which may explain its observed reactivity in the dark. While photodissociation of **3COT** has not been explored experimentally in solution owing to this instability,[24] the precursor performs exceptionally well in PACVD,[85] plausibly reflecting its markedly larger absorption cross section across the relevant spectral range (Fig. 6). Among the secondary channels, loss of COT from **2COT** (step 2.1) is also predicted to be a favourable route from the bright S_7 state (Table 3).

Precursors **3BuD** and **3MBuD** show the best PACVD performance alongside **3COT**,[85] while **3CHD** displays very similar photochemistry in solution studies[24] but somewhat poorer PACVD performance. The computed primary dissociation pathways for these three precursors are likewise closely related and are therefore discussed together. In contrast to the **3COT** (and **3CBuD**) cases, no substantial ligand relaxation is expected during Ru–diene elongation, and rigid scans show no instability of the GS wavefunction. The Ru–diene scans for **3BuD** and **3CHD** (Fig. 7) are nearly identical, consistent with their η^2-1,3-diene coordination, similar Frontier-orbital descriptions (Section 3.2), and common C_s symmetry (Fig. 3). The additional ring closure in CHD and the methyl substituent in **3MBuD** introduce only minor perturbations, as confirmed by scans and structures.

The GS Ru–diene BDEs for these three precursors (Table 3) are all close to 70 kcal mol^{-1} (3.0 eV). No diene loss in the dark was observed in solution photochemistry experiments, although **3MBuD** showed minimal deposition in the dark under PACVD conditions.[85] This is more plausibly attributed to thermal CO loss, as **3MBuD** also has the lowest Ru–CO BDE among the three, close to that of **3COT**.

Considering now the singlet excited states, only one relevant diene-loss pathway (step 2 in Fig. 2) emerges from the pristine precursors. For both **3BuD** and **3CHD**, the vertical excitation from the S_0 minimum (purple lines in Fig. 7) populates the bright S_2 state, which is the only allowed transition in the accessible spectral range. The Franck–Condon region lies at a slightly contracted Ru–diene distance from equilibrium, leading to excess vibrational energy. Near this region, S_1 and S_2 approach and cross (see insets in Fig. 7), as confirmed by NTO analysis (Fig. S11 and S13, SI). Rapid internal conversion can therefore populate S_1, which becomes nearly degenerate with the GS near the dissociation plateau. Although the NTOs do not evidence state inversion, the geometry may lie close to a crossing, and with sufficient vibrational energy the system is expected to proceed toward dissociation rather than deactivation. The effective pathway—photoexcitation to S_2, internal conversion to S_1, further Ru–diene elongation, and crossing to the GS surface—yields an effective dissociation barrier of *ca.* 45 kcal mol^{-1} (2 eV) (Table 3).

The main distinction among these precursors is in the position of the S_1–S_2 crossing relative to the S_0 equilibrium geometry: for **3BuD** (and **3MBuD**) the crossing occurs *ca.* 0.1 Å shorter than the equilibrium Ru–diene distance, whereas for **3CHD** it appears further away (*ca.* 0.2 Å). This difference results in a somewhat higher-energy crossing from the Franck–Condon region for **3CHD**, though whether this significantly alters relative reactivity remains unclear. Further insight will require non-adiabatic dynamics and time-resolved spectroscopy studies.

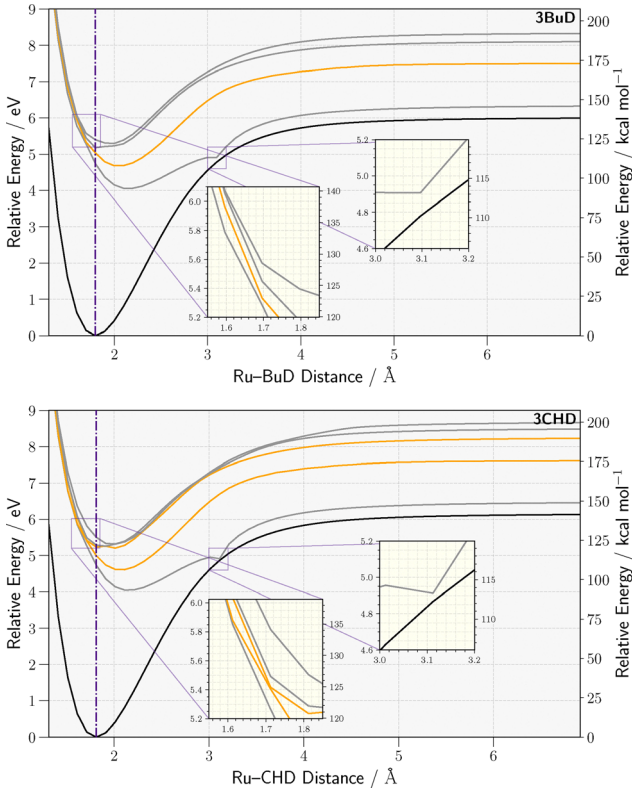

Fig. 7 Rigid scans of the Ru–BuD bond in **3BuD** and the Ru–CHD bond in **3CHD** corresponding to loss of diene *via* step 1 in Fig. 2. The scans were performed by distancing the diene from the metal along the line joining the metal to the centroid of the four carbon atoms connected to Ru. In each plot, a purple vertical line indicates vertical excitation from the GS equilibrium geometry. Black curve is the GS PES. Orange curves denote bright excited states, and grey curves denote dark excited states. Level of theory: TD-DFT/ωB97X-D3/def2-SVP,def2-TZVP(Ru)+ECP.

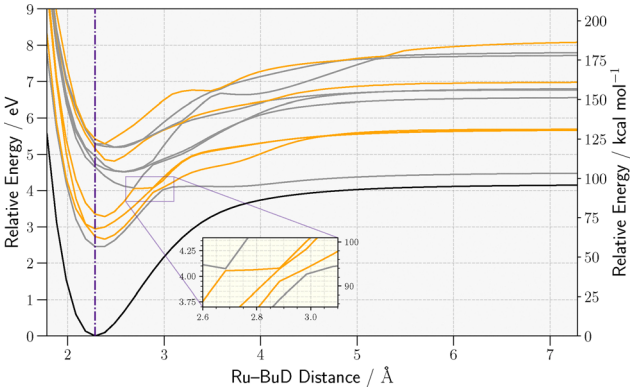

Fig. 8 Rigid scan of the Ru–BuD bond in **2BuD** corresponding to loss of diene *via* step 2.1 in Fig. 2. The scan was performed by increasing the Ru–diene distance along the line connecting the metal centre to the centroid of the four carbon atoms of the diene. The purple vertical line marks the vertical excitation from the GS equilibrium geometry. The black curve corresponds to the GS PES. Orange curves denote bright excited states, and grey curves denote dark excited states. Level of theory: TD-DFT/ωB97X-D3/def2-SVP,def2-TZVP(Ru)+ECP.

Subsequent diene-loss steps in the exhaustive dissociation of **3BuD** were also examined. After CO loss (step 2.1 in Fig. 2), rigid Ru–BuD scans reveal multiple crossings among S_1–S_5 and the GS near the dissociation plateau (Fig. 8). NTO analysis (Fig. S14, SI) confirms that the state labelled S_5 at the equilibrium geometry evolves into the lowest excited state at large Ru–diene distances. Although S_5 is dark, S_2–S_4 are bright and can lead to low-barrier dissociation through these crossings; the lowest effective barrier (from the S_4 minimum) is *ca.* 22 kcal mol^{-1} (1 eV). Diene loss from more CO-depleted fragments (steps 2.3 and 2.5) is unlikely owing to significantly higher barriers (Table 3; scans in Section S5.3, SI).

Finally, regarding **3CBuD**, this precursor shows no detectable diene loss in either extended photochemical experiments[24] or PACVD studies.[85] As discussed in Section 3.1, the coordinated ligand adopts a deltoid geometry in **3CBuD** and **2CBuD** but becomes square in **1CBuD** and **0CBuD**, while the free ligand is rectangular (D_{2h}). Elongation of the Ru–CBuD coordinate therefore leads to instabilities in rigid scans, with dark S_1 and S_2 states falling below the GS at larger distance (Section S5.5, SI). This occurs not only for the intact precursor but also for fragments formed after CO loss (steps 2.1, 2.3 and 2.5). NEB calculations connecting the intact structures to geometries with elongated Ru–CBuD bonds and relaxed D_{2h} ligands do not remove these instabilities but yield lower D_0 values than rigid scans overall (Fig. S17, SI). Given the rigidity of the CBuD ligand, alternative low-energy pathways appear unlikely, consistent with the absence of diene loss under both thermal and photochemical conditions.

3.5 Loss of CO from diene-containing fragments

The pathways for CO loss from pristine precursors and their diene-containing fragments (steps 1, 2.2, and 2.4 in Fig. 2) are influenced by the inequivalence of the CO ligands imposed by molecular symmetry. In the C_s precursors, one CO lies on the σ_h plane while the remaining two are out of plane and equivalent to each other. These small geometric differences lead to distinct PES profile and reactivities.

Three general scenarios emerge: (1) dissociation *via* a bright state that is dissociative or has a negligible barrier; (2) dissociation through an effective pathway involving internal conversion (IC) between excited states; and (3) absence of accessible excited-state channels, in which case thermal dissociation from the GS may compete. These situations are discussed below.

Direct CO loss through dissociative bright states (case 1) is found only for **3COT** and **3BuD**. In **3BuD**, any CO can dissociate through the low-lying S_2 state reached by an LF transition (Table 2). Fig. 9 shows a representative scan for an out-of-plane CO. The associated NTOs (Fig. 6) indicate a redistribution of density away from the Ru–CO bonding region, weakening the bond despite the absence of a strongly antibonding acceptor orbital. In **3COT**, only the CO lying in the σ_h plane dissociates *via* a bright state (S_4), populated by a mixed MLCT/LLCT transition (Table 2). The remaining two CO ligands lack dissociative bright states and therefore follow case 2 (see SI for scans). The NTOs (Fig. 6) reflect this asymmetry: the dominant excitation weakens the in-plane Ru–CO bond while

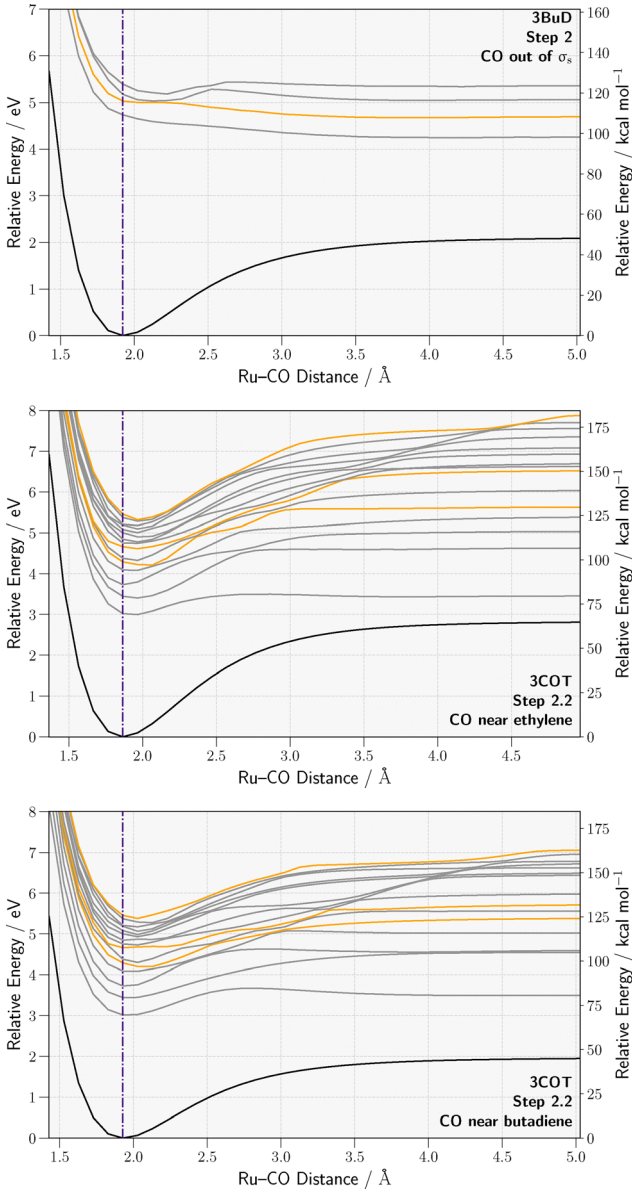

Fig. 9 Rigid scans of representative Ru–CO bonds in diene-containing molecules. The Ru–CO distance was contracted by 0.5 Å and elongated to ≈5.0 Å from the GS geometry in 0.1 Å increments. The purple vertical line marks vertical excitation from the GS equilibrium geometry. Black curves denote the GS PES. Orange curves denote bright excited states, and grey curves denote dark excited states. Level of theory: TD-DFT/ωB97X-D3/def2-SVP,def2-TZVP(Ru)+ECP.

maintaining or even reinforcing bonding for the out-of-plane CO ligands.

For **2COT** and **1COT**, CO loss does not proceed *via* dissociative excited states. In particular, dissociation of the CO adjacent to the out-of-plane ethylene moiety in **2COT** (step 2.2; Fig. 9, middle) and CO loss from **1COT** (step 2.4) correspond to case 3. In these systems, only relatively low barriers on the ground or excited state surfaces suggest possible thermal release (Table 3).

All remaining systems fall into case 2, where effective dissociation occurs through IC between excited states. Some channels require population of higher excited states. For example, removal of the CO opposite the ethylene unit in **2COT** requires excitation to S_7, followed by a cascade of IC steps leading to S_4, from which dissociation becomes accessible (Fig. 9, bottom). This contrasts with the lower-energy channel for the other CO in the same molecule discussed above (Fig. 9, middle).

Overall, CO loss from diene-containing species is generally accessible under photoexcitation, although its efficiency depends on the accessibility of bright states and IC pathways. This trend is consistent with solution-phase photochemistry, where higher CO yields are observed at shorter irradiation wavelengths.[24,85]

3.6 Total fragmentation of $Ru(CO)_3$

We end our survey discussing the loss of CO from $Ru(CO)_n$ (n = 1, 2, 3). For **3** (step 1.1; Fig. 2), dissociation is facilitated by several low-lying excited states, with S_4 providing the lowest direct barrier. An additional effective pathway originates from S_{12} and proceeds through S_9 *via* multiple internal conversions, yielding an overall barrier of only 12 kcal mol^{-1} (0.52 eV; Table 3). Subsequent CO loss from **2** (step 1.2) is less favourable. The lowest barrier from a bright state is 31 kcal mol^{-1} (1.34 eV), accessed from S_{12}, and no lower-barrier effective pathway involving internal conversion was identified. Although this barrier remains accessible at elevated temperatures, dissociation is expected to be slower than for **3**. For **1** (step 1.3), which has a triplet GS, dissociation proceeds through the lowest bright triplet state, T_9. This state connects to lower dark states and eventually to the GS near the dissociation plateau, where an unavoidable GS instability appears. The T_9 surface also provides the lowest direct dissociation barrier (23 kcal mol^{-1}, 1 eV). Its oscillator strength is modest (f = 0.0185), suggesting limited population and therefore a relatively slow dissociation rate if this channel dominates. Full scans for CO loss from all three fragments are provided in Section S5.6 in the SI.

3.7 A proposal of exhaustive dissociation pathways

This study provides a static analysis of the photodissociation landscape. Processes involving sequential ligand loss from fragments formed within a single photoabsorption event are not considered, as these require an explicit dynamical treatment. Such pathways may nonetheless contribute to the overall fragmentation pattern, as shown for iron carbonyl systems,[29,30,32,35] particularly for CO loss where several high-energy bright states with low barriers are available. Diene loss generally becomes less favourable at higher excitation energies, making cascading dissociation less likely. As some of the pathways involve internal conversion, their realisation depends on the probability of non-adiabatic transitions at crossing regions, which cannot be quantified within the present framework. While this may affect the relative probabilities of competing channels, the overall trends identified here, including the accessibility of low-barrier pathways, are expected to remain qualitatively valid. A more complete assessment would require

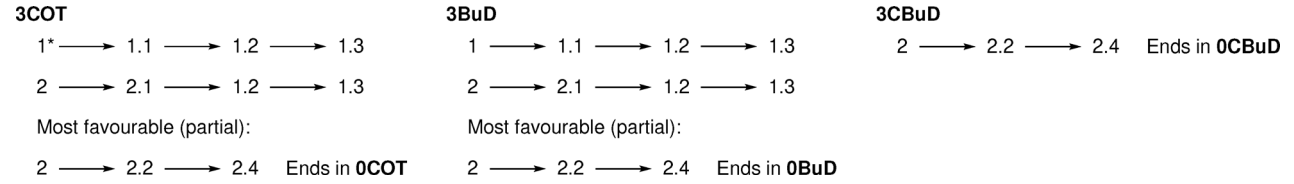

Fig. 10 Proposed dissociation channels derived from the present analysis. For **3COT** and **3BuD**, complete fragmentation to bare Ru can proceed through two main pathways: initial diene loss followed by successive CO loss, or initial CO loss followed by diene loss and further CO loss. These pathways correspond to steps 1 → 1.1 → 1.2 → 1.3 and 2 → 2.1 → 1.2 → 1.3, respectively. The most favourable dissociation pathways follow step 2 → 2.2 → 2.4, terminating in (diene)Ru fragments (**OCOT** and **OBuD**, respectively). In contrast, for **3CBuD**, only the sequence 2 → 2.2 → 2.4 is accessible, leading to (CBuD)Ru, with no viable route to complete fragmentation to bare Ru. See text for details. Numerical labels follow the definition in Fig. 2; * indicates channel also accessible *via* thermal dissociation from the ground state, consistent with experiment.

explicit treatment of non-adiabatic couplings and quantum dynamical simulations, which lies beyond the scope of the present work and will be addressed in future studies. The summary below therefore reflects only the pathways supported by the present analysis.

Fig. 10 collects the accessible channels leading to bare Ru or partially stripped fragments for **3COT**, **3BuD**, and **3CBuD.** In all cases, formation of (diene)Ru is the most accessible endpoint. For **3CBuD**, this is the only viable termination. Complete fragmentation to bare Ru is predicted for **3COT** and **3BuD** through similar sequences. For **3COT**, the pathway starting with step 1 may also proceed thermally as suggested by the lowest GS BDE and experimental observations. Along the alternative route, step 2.4 is more favourable for **3BuD** than for **3COT**, in line with the barriers in Table 3. Loss of diene from fragments containing one or no carbonyl is unlikely in all cases.

4 Conclusions

In this work, ground-state DFT scans and TD-DFT excited-state analyses were combined to examine the photodissociation pathways of (η^4-diene)Ru$(CO)_3$ precursors relevant to PACVD. For three representatives (**3COT**, **3BuD**, and **3CBuD**), complete fragmentation sequences towards bare Ru were mapped, enabling direct comparison of Ru–CO and Ru–diene cleavage channels within a consistent framework. The joint use of EDA–NOCV and NTO analyses connects the frontier-orbital character of the Ru–diene interaction with the accessibility of dissociative excited states and clarifies why certain ligands are preferentially lost under irradiation whereas others are retained. The calculated UV-vis spectra reproduce the overall position and intensity of the bands observed in solution-phase measurements. The transition assignments are consistent with previous analyses and provide a coherent basis for interpreting the photochemical trends across the series.

The results indicate that **3COT** and **3BuD** can access pathways leading to bare Ru under photoactivation, with closely related routes likely for **3CHD** and **3MBuD**, whereas **3CBuD** is expected to terminate at a stable (CBuD)Ru fragment. These differences can be traced to the topology of the low-lying excited states and to the degree of structural relaxation along the Ru–diene coordinate, which together control access to internal conversion regions and effective dissociative pathways, in line with photochemical and PACVD observations. The general conclusions are consistent with current experimental evidence and indicate that the participation of triplet states is likely to be minor, if any. In a strict sense, however, the results apply to the singlet manifold. A complete assessment of the role of triplet states would require explicit treatment of spin–orbit coupling and non-adiabatic effects.

Although the present treatment is static and does not address the full excited-state dynamics, the mapped potential energy surfaces delineate the regions where bond weakening and cleavage become accessible. The use of NEB calculations accounts for the principal structural relaxation of the COT and CBuD ligands beyond rigid bond stretching, although additional nuclear degrees of freedom are not explicitly explored. The dissociation profiles obtained here therefore provide an initial map and quantitative basis for future dynamical simulations for parametrising multiscale models of PACVD growth, helping bridge molecular-level photochemistry with predictive descriptions of photo-assisted nanofabrication processes that can be directly compared with deposition experiments.

Author contributions

C. P. S.: methodology; software; validation; formal analysis; investigation; data curation; writing – original draft; writing – review & editing; visualisation. A. V. V.: methodology; writing – review & editing; supervision; funding acquisition. A. V. W.: resources; writing – review & editing. N. J. M.: writing – review & editing; supervision; funding acquisition. A. V. S.: writing – review & editing; supervision; funding acquisition. L. M.-W.: resources; writing – review & editing. M. Z.: conceptualization; methodology; investigation; writing – review & editing; visualization; supervision. F. F.: conceptualization; methodology; writing – original draft; writing – review & editing; supervision; project administration; funding acquisition.

Conflicts of interest

There are no conflicts to declare.

Data availability

The data that support the findings of this study are available within the article and its supplementary information (SI).

Additional data are available from the corresponding authors upon reasonable request. Supplementary information: additional computational details and supporting figures/tables (structures, spectra/NTO assignments, dissociation scans, and Cartesian coordinates). See DOI: https://doi.org/10.1039/d6cp00843g.

Acknowledgements

This work was supported by the RADON project (Grant Agreement No. 872494) within the H2020-MSCA-RISE-2019 call and COST Action CA20129 (MultIChem) together with Innovators Grant IG20129 (INDICO), both supported by COST (European Cooperation in Science and Technology). C. P. S. acknowledges support from the Engineering and Physical Sciences Research Council (EPSRC) under Grant No. EP/W52461X/1. L. M.-W. and A. V. W. gratefully acknowledge support from the National Science Foundation under the collaborative grants DMR-2216070 and DMR-2216069. F. F. acknowledges support from the Royal Society ISPF International Collaboration Awards 2024 (Brazil and South Africa) under Grant No. ICAO\R1\241112 for the NUBIAN project. M. Z. acknowledges support from the Science Fund of the Republic of Serbia (#7750288) and the Ministry of Science, Technological Development, and Innovation of the Republic of Serbia (Contract No. 451-03-33/2026-03/200026). The authors thank Dr Timothy Kinnear for continued HPC support.

References

1 A. C. Jones and M. L. Hitchman, *Chemical Vapour Deposition: Precursors, Processes and Applications*, The Royal Society of Chemistry, 2008.
2 R. Gaur, L. Mishra, M. A. Siddiqi and B. Atakan, *RSC Adv.*, 2014, **4**, 33785–33805.
3 S. Barth, M. Huth and F. Jungwirth, *J. Mater. Chem. C*, 2020, **8**, 15884–15919.
4 I. Utke, P. Swiderek, K. Höflich, K. Madajska, J. Jurczyk, P. Martinović and I. Szymańska, *Coord. Chem. Rev.*, 2022, **458**, 213851.
5 J.-C. Yu, M. K. Abdel-Rahman, D. H. Fairbrother and L. McElwee-White, *ACS Appl. Mater. Interfaces*, 2021, **13**, 48333–48348.
6 P. Wang, Y. Huan, P. Yang, M. Cheng, J. Shi and Y. Zhang, *Acc. Mater. Res.*, 2021, **2**, 751–763.
7 T. Kang, T. W. Tang, B. Pan, H. Liu, K. Zhang and Z. Luo, *ACS Mater. Au*, 2022, **2**, 665–685.
8 J. R. Creighton and J. E. Parmeter, *Crit. Rev. Solid State Mater. Sci.*, 1993, **18**, 175–237.
9 M. L. Green and R. A. Levy, *JOM*, 1985, **37**, 63–71.
10 G. Zhang, F. R. Lin, F. Qi, T. Heumüller, A. Distler, H.-J. Egelhaaf, N. Li, P. C. Y. Chow, C. J. Brabec, A. K.-Y. Jen and H.-L. Yip, *Chem. Rev.*, 2022, **122**, 14180–14274.
11 J. Janata and M. Josowicz, *Nat. Mater.*, 2003, **2**, 19–24.
12 R. L. Carroll and C. B. Gorman, *Angew. Chem., Int. Ed.*, 2002, **41**, 4378–4400.
13 R. H. Friend, R. W. Gymer, A. B. Holmes, J. H. Burroughes, R. N. Marks, C. Taliani, D. D. C. Bradley, D. A. D. Santos, J. L. Brédas, M. Lögdlund and W. R. Salaneck, *Nature*, 1999, **397**, 121–128.
14 B. Luo and W. L. Gladfelter, *Chemical Vapour Deposition: Precursors, Processes and Applications*, The Royal Society of Chemistry, 2008, ch. 7, pp. 320–356.
15 Q. Wang, J. G. Ekerdt, D. Gay, Y.-M. Sun and J. M. White, *Appl. Phys. Lett.*, 2004, **84**, 1380–1382.
16 U. Banik, M. T. U. Malik, S. M. S. M. Rahat and A. K. Mallik, *Energy Storage*, 2023, **5**, e380.
17 D.-S. Yoon, J. S. Roh, H. K. Baik and S.-M. Lee, *Crit. Rev. Solid State Mater. Sci.*, 2002, **27**, 143–226.
18 O. Chyan, T. N. Arunagiri and T. Ponnuswamy, *J. Electrochem. Soc.*, 2003, **150**, C347.
19 R. Chan, T. N. Arunagiri, Y. Zhang, O. Chyan, R. M. Wallace, M. J. Kim and T. Q. Hurd, *Electrochem. Solid State Lett.*, 2004, **7**, G154.
20 K. R. Johnson, P. Arevalo Rodriguez, C. R. Brewer, J. A. Brannaka, Z. Shi, J. Yang, B. Salazar, L. McElwee-White and A. V. Walker, *J. Chem. Phys.*, 2017, **146**, 052816.
21 H. Haick and D. Cahen, *Prog. Surf. Sci.*, 2008, **83**, 217–261.
22 B. G. Salazar, C. R. Brewer, L. McElwee-White and A. V. Walker, *J. Vac. Sci. Technol., A*, 2022, **40**, 023404.
23 C. R. Brewer, O. M. Hawkins, N. C. Sheehan, J. D. Bullock, V. D. Kleiman, A. V. Walker and L. McElwee-White, *Organometallics*, 2019, **38**, 4363–4370.
24 C. R. Brewer, N. C. Sheehan, J. Herrera, A. V. Walker and L. McElwee-White, *Organometallics*, 2022, **41**, 761–775.
25 The term diene is used here as a shorthand descriptor for the η^4-bound unsaturated hydrocarbon ligand in this precursor family. Although cyclooctatetraene is formally a tetraene, only two of its double bonds are involved in the η^4 interaction with Ru, so it is retained under the general notation (η^4-diene)Ru(CO)$_3$.
26 O. Jaenicke, R. Kerber, P. Kirsch, E. von Gustorf and R. Rumin, *J. Organomet. Chem.*, 1980, **187**, 361–373.
27 V. Bachler, F.-W. Grevels, K. Kerpen, G. Olbrich and K. Schaffner, *Organometallics*, 2003, **22**, 1696–1711.
28 T. H. Chang and J. I. Zink, *Inorg. Chem.*, 1985, **24**, 4016–4019.
29 N. Leadbeater, *Coord. Chem. Rev.*, 1999, **188**, 35–70.
30 S. A. Trushin, W. Fuss, K. L. Kompa and W. E. Schmid, *J. Phys. Chem. A*, 2000, **104**, 1997–2006.
31 J. J. Turner, M. W. George, M. Poliakoff and R. N. Perutz, *Chem. Soc. Rev.*, 2022, **51**, 5300–5329.
32 L. Bañares, T. Baumert, M. Bergt, B. Kiefer and G. Gerber, *J. Chem. Phys.*, 1998, **108**, 5799–5811.
33 B. Andreides, A. V. Verkhovtsev, J. Fedor and A. V. Solov'yov, *J. Phys. Chem. A*, 2023, **127**, 3757–3767.
34 K. Nagamori, M. Haze, H. Nakata, O. Zingsheim, K. Yamasaki and H. Kohguchi, *J. Phys. Chem. A*, 2022, **126**, 306–313.

35 J. Troß, J. E. Arias-Martinez, K. Carter-Fenk, N. C. Cole-Filipiak, P. Schrader, L. M. McCaslin, M. Head-Gordon and K. Ramasesha, *J. Am. Chem. Soc.*, 2024, **146**, 22711–22723.
36 Z.-F. Zhang and M.-D. Su, *RSC Adv.*, 2019, **9**, 2626–2640.
37 P. L. Bogdan and E. Weitz, *J. Am. Chem. Soc.*, 1989, **111**, 3163–3167.
38 J. Li, G. Schreckenbach and T. Ziegler, *J. Am. Chem. Soc.*, 1995, **117**, 486–494.
39 M. Zlatar, M. Allan and J. Fedor, *J. Phys. Chem. C*, 2016, **120**, 10667–10674.
40 C. P. Souza and F. Fantuzzi, in *Organometallic Chemistry*, ed. C. Bakewell, N. Costa, R. Musgrave and G. Owen, Royal Society of Chemistry, 2024, vol. 45, pp. 271–316.
41 C. P. Souza, A. V. Verkhovtsev, N. J. Mason, A. V. Solov'yov and F. Fantuzzi, *J. Chem. Phys.*, 2025, **163**, 094704.
42 G. B. Sushko, I. A. Solov'yov, A. V. Verkhovtsev, S. N. Volkov and A. V. Solov'yov, *Eur. Phys. J. D*, 2016, **70**, 12.
43 G. B. Sushko, I. A. Solov'yov and A. V. Solov'yov, *Eur. Phys. J. D*, 2016, **70**, 217.
44 A. V. Verkhovtsev, I. A. Solov'yov and A. V. Solov'yov, *Eur. Phys. J. D*, 2021, **75**, 213.
45 I. A. Solov'yov, A. V. Yakubovich, P. V. Nikolaev, I. Volkovets and A. V. Solov'yov, *J. Comput. Chem.*, 2012, **33**, 2412–2439.
46 A. V. Solov'yov, A. V. Verkhovtsev, N. J. Mason, R. A. Amos, I. Bald, G. Baldacchino, B. Dromey, M. Falk, J. Fedor, L. Gerhards, M. Hausmann, G. Hildenbrand, M. Hrabovský, S. Kadlec, J. Kočišek, F. Lépine, S. Ming, A. Nisbet, K. Ricketts, L. Sala, T. Schlathölter, A. E. H. Wheatley and I. A. Solov'yov, *Chem. Rev.*, 2024, **124**, 8014–8129.
47 P. de Vera, M. Azzolini, G. Sushko, I. Abril, R. Garcia-Molina, M. Dapor, I. A. Solov'yov and A. V. Solov'yov, *Sci. Rep.*, 2020, **10**, 20827.
48 P. de Vera, A. Verkhovtsev, G. Sushko and A. V. Solov'yov, *Eur. Phys. J. D*, 2019, **73**, 215.
49 A. Prosvetov, A. V. Verkhovtsev, G. Sushko and A. V. Solov'yov, *Phys. Chem. Chem. Phys.*, 2022, **24**, 10807–10819.
50 A. Prosvetov, A. V. Verkhovtsev, G. Sushko and A. V. Solov'yov, *Beilstein J. Nanotechnol.*, 2021, **12**, 1151–1172.
51 A. Prosvetov, A. V. Verkhovtsev, G. Sushko and A. V. Solov'yov, *Eur. Phys. J. D*, 2023, **77**, 15.
52 H. Lyshchuk, A. V. Verkhovtsev, J. Kočišek, J. Fedor and A. V. Solov'yov, *J. Phys. Chem. A*, 2025, **129**, 2016–2023.
53 J.-D. Chai and M. Head-Gordon, *J. Chem. Phys.*, 2008, **128**, 084106.
54 S. Grimme, J. Antony, S. Ehrlich and H. Krieg, *J. Chem. Phys.*, 2010, **132**, 154104.
55 F. Weigend and R. Ahlrichs, *Phys. Chem. Chem. Phys.*, 2005, **7**, 3297–3305.
56 M. J. Frisch, G. W. Trucks, H. B. Schlegel, G. E. Scuseria, M. A. Robb, J. R. Cheeseman, G. Scalmani, V. Barone, G. A. Petersson, H. Nakatsuji, X. Li, M. Caricato, A. V. Marenich, J. Bloino, B. G. Janesko, R. Gomperts, B. Mennucci, H. P. Hratchian, J. V. Ortiz, A. F. Izmaylov, J. L. Sonnenberg, D. Williams-Young, F. Ding, F. Lipparini, F. Egidi, J. Goings, B. Peng, A. Petrone, T. Henderson, D. Ranasinghe, V. G. Zakrzewski, J. Gao, N. Rega, G. Zheng, W. Liang, M. Hada, M. Ehara, K. Toyota, R. Fukuda, J. Hasegawa, M. Ishida, T. Nakajima, Y. Honda, O. Kitao, H. Nakai, T. Vreven, K. Throssell, J. A. Montgomery, Jr., J. E. Peralta, F. Ogliaro, M. J. Bearpark, J. J. Heyd, E. N. Brothers, K. N. Kudin, V. N. Staroverov, T. A. Keith, R. Kobayashi, J. Normand, K. Raghavachari, A. P. Rendell, J. C. Burant, S. S. Iyengar, J. Tomasi, M. Cossi, J. M. Millam, M. Klene, C. Adamo, R. Cammi, J. W. Ochterski, R. L. Martin, K. Morokuma, O. Farkas, J. B. Foresman and D. J. Fox, *Gaussian 16 Revision A.03*, Gaussian Inc., Wallingford CT, 2016.
57 G. Henkelman and H. Jónsson, *J. Chem. Phys.*, 2000, **113**, 9978–9985.
58 F. Neese, *Wiley Interdiscip. Rev.:Comput. Mol. Sci.*, 2022, **12**, e1606.
59 S. Grimme, S. Ehrlich and L. Goerigk, *J. Comput. Chem.*, 2011, **32**, 1456–1465.
60 F. Weigend, *Phys. Chem. Chem. Phys.*, 2006, **8**, 1057–1065.
61 V. Ásgeirsson, B. O. Birgisson, R. Bjornsson, U. Becker, F. Neese, C. Riplinger and H. Jónsson, *J. Chem. Theory Comput.*, 2021, **17**, 4929–4945.
62 R. L. Martin, *J. Chem. Phys.*, 2003, **118**, 4775–4777.
63 F. Plasser and H. Lischka, *J. Chem. Theory Comput.*, 2012, **8**, 2777–2789.
64 F. Plasser, *J. Chem. Phys.*, 2020, **152**, 084108.
65 R. C. Hilborn, *Am. J. Phys.*, 1982, **50**, 982–986.
66 M. P. Mitoraj, A. Michalak and T. Ziegler, *J. Chem. Theory Comput.*, 2009, **5**, 962–975.
67 G. te Velde, F. M. Bickelhaupt, E. J. Baerends, C. Fonseca Guerra, S. J. A. van Gisbergen, J. G. Snijders and T. Ziegler, *J. Comput. Chem.*, 2001, **22**, 931–967.
68 E. J. Baerends, N. F. Aguirre, N. D. Austin, J. Autschbach, F. M. Bickelhaupt, R. Bulo, C. Cappelli, A. C. T. van Duin, F. Egidi, C. Fonseca Guerra, A. Förster, M. Franchini, T. P. M. Goumans, T. Heine, M. Hellström, C. R. Jacob, L. Jensen, M. Krykunov, E. van Lenthe, A. Michalak, M. M. Mitoraj, J. Neugebauer, V. P. Nicu, P. Philipsen, H. Ramanantoanina, R. Rüger, G. Schreckenbach, M. Stener, M. Swart, J. M. Thijssen, T. Trnka, L. Visscher, A. Yakovlev and S. van Gisbergen, *J. Chem. Phys.*, 2025, **162**, 162501.
69 C. Adamo and V. Barone, *J. Chem. Phys.*, 1999, **110**, 6158–6170.
70 E. Caldeweyher, S. Ehlert, A. Hansen, H. Neugebauer, S. Spicher, C. Bannwarth and S. Grimme, *J. Chem. Phys.*, 2019, **150**, 154122.
71 E. Van Lenthe and E. J. Baerends, *J. Comput. Chem.*, 2003, **24**, 1142–1156.
72 E. V. Lenthe, E. J. Baerends and J. G. Snijders, *J. Chem. Phys.*, 1993, **99**, 4597–4610.
73 M. I. Bruce, K. Costuas, T. Davin, B. G. Ellis, J.-F. Halet, C. Lapinte, P. J. Low, M. E. Smith, B. W. Skelton, L. Toupet and A. H. White, *Organometallics*, 2005, **24**, 3864–3881.
74 R. Salzmann, C. J. Ziegler, N. Godbout, M. T. McMahon, K. S. Suslick and E. Oldfield, *J. Am. Chem. Soc.*, 1998, **120**, 11323–11334.
75 S. Gückel, J. B. G. Gluyas, S. El-Tarhuni, A. N. Sobolev, M. W. Whiteley, J.-F. Halet, C. Lapinte, M. Kaupp and P. J. Low, *Organometallics*, 2018, **37**, 1432–1445.

76 B. Dickens and W. N. Lipscomb, *J. Chem. Phys.*, 1962, **37**, 2084–2093.
77 M. A. Bennett, H. Neumann, A. C. Willis, V. Ballantini, P. Pertici and B. E. Mann, *Organometallics*, 1997, **16**, 2868–2878.
78 E. R. Davidson, K. L. Kunze, F. B. C. Machado and S. J. Chakravorty, *Acc. Chem. Res.*, 1993, **26**, 628–635.
79 G. Frenking, I. Fernández, N. Holzmann, S. Pan, I. Krossing and M. Zhou, *JACS Au*, 2021, **1**, 623–645.
80 A. Krapp, K. K. Pandey and G. Frenking, *J. Am. Chem. Soc.*, 2007, **129**, 7596–7610.
81 W. Kennedy, V. Pattathil, Y. Wei, F. Fantuzzi and C. Pranckevicius, *J. Am. Chem. Soc.*, 2025, **147**, 3500–3506.
82 G. Ganguly, S. Pathak and A. Paul, *Phys. Chem. Chem. Phys.*, 2021, **23**, 16005–16012.
83 P. B. Karadakov, *J. Phys. Chem. A*, 2008, **112**, 7303–7309.
84 F. Fantuzzi, T. M. Cardozo and M. A. C. Nascimento, *ChemPhysChem*, 2016, **17**, 288–295.
85 C. R. Brewer, B. Das, R. Singh, D. Caretti, D. Bhattacharyya, O. Oni, X. Kang, J. Perry, L. McElwee-White and A. V. Walker, *ACS Appl. Mater. Interfaces*, 2025, **17**, 55034–55044.

